Journal of Fluids and Structures 17 (2003) 243–259

JOURNAL OF FLUIDS AND STRUCTURES

www.elsevier.nl/locate/jnlabr/yjfls

A theoretical and experimental investigation of the effects of a steady angle of attack on the nonlinear flutter of a delta wing plate model

P.J. Attar*, E.H. Dowell, D.M. Tang

Department of Mechanical Engineering and Materials Science, Duke University, Box 90300, Durham, NC, 27708-0300, USA

Received 2 April 2001; accepted 18 July 2002

Abstract

Limit cycle oscillations (LCO) of wings on certain modern high performance aircraft have been observed in flight and in wind tunnel experiments. Whether the physical mechanism that gives rise to this behavior is a fluid or structural nonlinearity or both is still uncertain. It has been shown that an aeroelastic theoretical model with only a structural nonlinearity can predict accurately the limit cycle behavior at low subsonic flow for a plate-like wing at zero angle of attack. Changes in the limit cycle and flutter behavior as the angle of attack is varied have also been observed in flight. It has been suggested that this sensitivity to angle of attack is due to a fluid nonlinearity. In this investigation, we study the flutter and limit cycle behavior of a wing in low subsonic flow at small steady angles of attack. Experimental results are compared to those predicted using an aeroelastic theoretical model with only a structural nonlinearity. Results from both experiment and theory show a change in flutter speed as the steady angle of attack is varied. Also the LCO magnitude increased *at a given velocity* as the angle of attack was increased for both the experiment and theory. While not proving that the observed sensitivity to angle of attack of LCO in aircraft is due to a structural nonlinearity, the results do show that a change in the aeroelastic behavior at angles of attack can be caused by a structural nonlinearity as well as a fluid nonlinearity. In this paper, only structural nonlinearities are considered, but an extension to include aerodynamic nonlinearities would be very worthwhile.

1. Introduction

Flutter and the nonlinear limit cycle behavior of flat, low-aspect ratio plates at zero angle of attack have recently been studied (Doggett and Solstmann, 1989; Tang et al., 1999a,b; Weiliang and Dowell, 1991). In Doggett and Solstmann (1989) and Tang et al. (1999a), it was shown experimentally that limit cycles do exist for plates that are only constrained along one edge. It has been determined that limit cycle oscillations (LCO) can be accurately predicted using a nonlinear plate theory (Tang et al., 1999a,b; Weiliang and Dowell, 1991). Tang and Dowell (2001) performed a theoretical study which examined how a nonzero angle of attack will affect the flutter and limit cycle results. It was found that an angle of attack indeed changes the nonlinear aeroelastic behavior of the wing.

In the present paper, this nonzero angle of attack behavior will be studied further both theoretically and experimentally. Results from a theoretical model similar to the one utilized in Tang and Dowell (2001) will be compared with the results of experiment. The theoretical model consists of a reduced order aerodynamic model constructed from an unsteady vortex lattice code along with a nonlinear structural plate model which is represented via Lagrange's

*Corresponding author. Fax: +1-919-660-8963.
E-mail address: pja@acpub.duke.edu (P.J. Attar).

0889-9746/03/$ - see front matter
PII: S0889-9746(02)00123-8

Nomenclature

a	delta wing root chord dimension
a_m,b_n	in-plane generalized coordinates
b	delta wing trailing edge span dimension
D	plate flexural rigidity term defined as $Eh^3/[12(1-v^2)]$
E	modulus of elasticity
$[E]$	matrix which describes aerodynamic downwash as a function of plate structural modes
F_N	forcing due to structural geometric nonlinearity
h	delta wing plate thickness
km	number of vortex panels on the plate in the streamwise direction
kn	number of vortex panels on the plate in the spanwise direction
kmm	total number of vortex panels on the plate and in the wake in the streamwise direction
kmn	total number of vortex panels on the wing
knx	total number of vortex panels on wing and in the wake
mxy,nxy	total number of in-plane and out-of-plane structural natural modes retained in the aeroelastic model
m_p	delta wing mass per unit area
$\bar{q}, \bar{a}, \bar{b}$	nondimensional generalized coordinates
q_o	out-of-plane generalized coordinate
$\bar{Q}_o^p$	nondimensional generalized aerodynamic loading
Ra	number of aerodynamic eigenmodes used in analysis
$[T]$	mesh transfer matrix
u,v	in-plane plate deflections
U	flow velocity
w	out-of-plane plate deflection
$[W]$	discrete out-of-plane modal vector matrix
x,y	streamwise and spanwise position coordinates
$[X]$, $[Y]$	right and left aerodynamic eigenvector matrices
z	position coordinate normal(perpendicular) to undeformed plate
$[Z]$	aerodynamic eigenvalue matrix
z_i	imaginary part of aerodynamic eigenvalue
z_r	real part of aerodynamic eigenvalue

Greek letters

α, β	in-plane modal functions
α_0	prescribed angle of attack at root chord of wing
γ	aerodynamic modal coordinates
Γ	vortex strength
Δt	time step
Δx	plate vortex element length in streamwise direction
θ	plate structural state-space vector
v	Poisson's ratio
ξ_o,ω_o	modal damping and modal frequency
ρ_∞	flow density
τ	term which arises from nondimensionalization defined as $\tau = Db/a^3$
ϕ	out-of-plane modal functions

equations. A perturbation, aeroelastic model is constructed in order to calculate the flutter results for a nonzero angle of attack. Time simulation is used to determine the calculated LCO.

2. Theoretical formulation

An abbreviated discussion is presented here. For more details, see Tang and Dowell (2001).

2.1. Structural model

The delta wing is modelled as a thin plate. The structural theory is the dynamic version of the nonlinear plate equations attributed to von Karman. It includes higher order terms in the strain–displacement relations and does not include any transverse shearing effects. The kinetic and strain energies are expressed in terms of modal expansions of the in-plane and out-of-plane plate deflections. Finally, Lagrange's equations are used to derive equations for the modal coordinates. In the strain and kinetic energies, the in-plane inertia terms have been neglected and the plate is assumed to have a constant thickness h (Tang and Dowell, 2001).

The plate deflections in the out-of-plane and in-plane directions can then be represented as

$$u(x,y,t) = \sum_m a_m(t)\alpha_m(x,y) \quad m = 1 \cdot mxy, \tag{1}$$

$$v(x,y,t) = \sum_n b_n(t)\beta_n(x,y) \quad n = 1 \cdot mxy, \tag{2}$$

$$w(x,y,t) = \sum_o q_o(t)\phi_o(x,y) \quad o = 1 \cdot nxy, \tag{3}$$

where the modal functions α, β, and ϕ are calculated using the commercial finite element package ANSYS (ANSYS User Manual, 1998). The finite element model which is used to calculate the modal functions contains 900 elements. The element used is a 4-node shell element. To determine the out-of-plane modal functions, the model is fully constrained along a partial portion of the root chord and allowed to displace and rotate freely at all other portions of the wing.

Two different boundary conditions are used to find two different sets of in-plane modal functions (only one boundary was considered in Tang and Dowell, 2001). The first is that of zero displacement or fully constrained as in Tang and Dowell (2001). The second alternative boundary condition is that the wing is allowed to displace essentially freely in the in-plane direction (there is a very soft in-plane spring at the root) at the root chord, but the motion in the out-of-plane direction is fully constrained or clamped. All other points on the wing are unconstrained. As will be shown, the softer in-plane boundary condition more accurately models the experimental results.

The in-plane equations of motion can be found by placing the modal expansions in Eqs. (1)–(3) into the strain energy and then using Lagrange's equation. Note that all of the aerodynamic loading occurs in the out-of-plane direction. The nondimensional in-plane equations of motion become (Tang and Dowell, 2001)

a_m:

$$\sum_i \bar{a}_i A1_{im} + \sum_j \bar{b}_j B1_{jm} = \sum_l \sum_o \bar{q}_l \bar{q}_o C1_{lom}; \tag{4}$$

b_n:

$$\sum_i \bar{a}_i A2_{in} + \sum_j \bar{b}_j B2_{jn} = \sum_l \sum_o \bar{q}_l \bar{q}_o C2_{lon}. \tag{5}$$

Similarly, the nondimensional out-of-plane equations of motion become

$$\ddot{\bar{q}}_o + 2\xi_o \omega_o \dot{\bar{q}}_o + \omega_o^2 \bar{q}_o + \tau\left(\sum_m \sum_l \bar{a}_m \bar{q}_l K1_{mlo} + \sum_n \sum_l \bar{b}_n \bar{q}_l K2_{nlo} + \sum_r \sum_s \sum_t \bar{q}_r \bar{q}_s \bar{q}_t K3_{rsto}\right) + \bar{Q}_o^P = 0, \tag{6}$$

where in the above equations the coefficients multiplying the modal coordinates depend upon the modal functions (see Tang and Dowell (2001) for details), τ is a constant that arises from the nondimensionalization (see the Nomenclature) and ω_o and ξ_o are the modal frequencies and damping, respectively. $\bar{Q}_o^P$ is the nondimensional generalized aerodynamic loading, which will be discussed next.

2.2. Aerodynamic model

The flow is assumed to be inviscid, incompressible and irrotational. Therefore, a linear unsteady potential flow solution is used here based upon the unsteady vortex lattice model (Hall, 1994). The vortex lattice mesh used in the numerical analysis is shown in Fig. 1. Vortex elements are placed on the wing and in the wake and point vortices are placed at the quarter chord of each element. At the three-quarter chord of each element on the wing a collocation point is placed where the boundary condition on the wing must be satisfied. Following Hall (1994), the aerodynamic model is

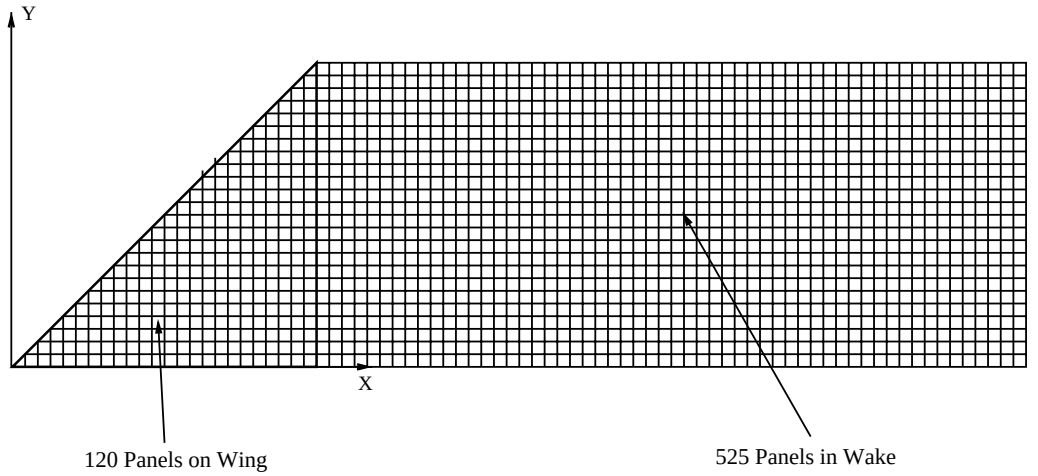

Fig. 1. Computational mesh used in the vortex lattice model.

of the form

$$w_i^{t+1} = \sum_{j=1}^{knx} K_{ij}\Gamma_j^{t+1}, \quad i = 1,..\, kmn, \tag{7}$$

where w_i^{t+1} is the downwash at time step $t+1$ at a certain streamwise and spanwise location i on the wing, Γ_j^{t+1} is the strength of the jth point vortex at the time step $t+1$ and K_{ij} is the aerodynamic kernel function (see Katz and Plotkin (2001) for derivation of this equation. In the wake, there are two relations based on the Kelvin condition that the angular momentum and therefore the vorticity around the wing and wake is conserved. At the first vortex in the wake, and at a certain spanwise location, we have

$$\Gamma_{km+1}^{t+1} = -\sum_{j}^{km}(\Gamma_j^{t+1} - \Gamma_j^t). \tag{8}$$

Once the vorticity has been shed into the wake, it is convected with speed U,

$$\Gamma_i^{t+1} = \Gamma_{i-1}^t, \quad i = km+2,.., kmm-1. \tag{9}$$

Finally, for the last point in the wake, the starting vortex, we have

$$\Gamma_i^{t+1} = \Gamma_{i-1}^t + \alpha\Gamma_i^t, \quad i = kmm, \tag{10}$$

where α is the wake relaxation factor and is usually between 0.95 and 1.0. Expressing Eqs. (7)–(10) in matrix form gives

$$A\Gamma^{t+1} + B\Gamma^t = w^{t+1}. \tag{11}$$

The nondimensional generalized aerodynamic loading $\bar{Q}_o^P$ is defined as

$$\bar{Q}_o^P = \frac{ab}{h}\int\int \Delta\bar{p}\phi_o \,\mathrm{d}\bar{x}\,\mathrm{d}\bar{y}, \tag{12}$$

where the nondimensional pressure distribution $\Delta\bar{p}$ at a certain spanwise and chordwise location can be obtained from the unsteady Bernoulli equation

$$\Delta\bar{p}_j = \frac{U^2\rho_\infty a}{\Delta x}\left[(\Gamma_j^{t+1} + \Gamma_j^t)/2 + \sum_{i}^{j}(\Gamma_i^{t+1} - \Gamma_i^t)\right]. \tag{13}$$

2.3. Aeroelastic state-space equations

Since the aerodynamic system is modelled using a discrete time formulation, the structural equations are put into that form as well (for details, see Tang and Dowell, 2001).

The downwash, w^{t+1} can be written as a function of the state of the plate

$$\{w(x,y)\}^{t+1} = \frac{h}{U}[T][W(x,y)]\{\dot{\bar{q}}\}^{t+1} + \frac{h}{a}[T]\left[\frac{\partial W(x,y)}{\partial x}\right]\{\bar{q}\}^{t+1} + [T]\{\alpha_0\} = [T][E]\{\theta\} + [T]\{\alpha_0\}, \tag{14}$$

where $[T]$ is a transformation matrix that accounts for the difference in the structural finite element mesh which was used to compute the spatial modal functions and the vortex lattice aerodynamic mesh. $[W]$ is the matrix of discrete structural modal vectors. Note that α_0 in Eq. (14) represents the angle of attack of the root chord of the wing which is prescribed in both the theory and the experiment.

Eqs. (6), (11) and (14) can be put in state-space matrix form, viz.

$$\begin{bmatrix} A & -TE \\ C_2 & D_2 \end{bmatrix}\begin{Bmatrix} \Gamma \\ \theta \end{Bmatrix}^{t+1} + \begin{bmatrix} B & 0 \\ C_1 & D_1 \end{bmatrix}\begin{Bmatrix} \Gamma \\ \theta \end{Bmatrix}^{t} = \begin{Bmatrix} T\alpha_0 \\ -F_N \end{Bmatrix}^{t}. \tag{15}$$

2.4. Reduced order aeroelastic model

The vortex lattice aerodynamic model may be "reduced" using aerodynamic eigenmodes (Hall, 1994). To accomplish this, a transformation from the original flow variables Γ to the modal variables γ is made:

$$\Gamma = X_{Ra}\gamma, \tag{16}$$

where the value Ra signifies the number of aerodynamic modal vectors kept in the matrix of aerodynamic eigenvectors X. In practice, Ra is much less than the dimension of the full vortex lattice model. Figs. 2 and 3 show the aerodynamic eigenvalues calculated from the vortex lattice model with a total of 645 vortex elements, 120 on the plate and 525 in the wake. The number of aerodynamic eigenmodes retained in the reduced order model (ROM) is 7.

Thus the reduced aeroelastic model has the form (Tang and Dowell, 2001)

$$\begin{bmatrix} I & -Y_{Ra}^T TE \\ C_2 X_{Ra} & D_2 \end{bmatrix}\begin{Bmatrix} \gamma \\ \theta \end{Bmatrix}^{t+1} + \begin{bmatrix} -Z_{Ra} & 0 \\ C_1 X_{Ra} & D_1 \end{bmatrix}\begin{Bmatrix} \gamma \\ \theta \end{Bmatrix}^{t} = \begin{Bmatrix} Y_{Ra}^T T\alpha_0 \\ -F_N \end{Bmatrix}^{t}. \tag{17}$$

In order to accelerate the convergence of the aerodynamic eigenvector expansion, a quasi-static solution is also added to the reduced order model (see Tang and Dowell (2001) and Hall (1994) for more details on this procedure).

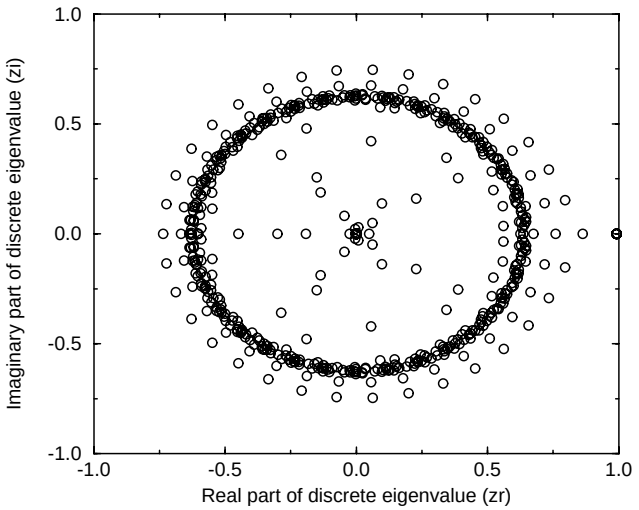

Fig. 2. Discrete time aerodynamic eigenvalues.

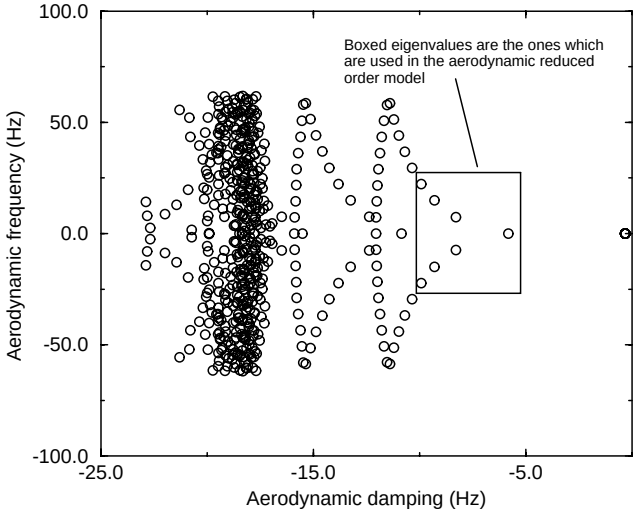

Fig. 3. Continuous time aerodynamic eigenvalues.

2.5. Perturbation solution

If the steady angle of attack α_0 is zero, the flutter solution can be found by setting F_N to zero and solving the corresponding aeroelastic eigenvalue problem. However, if α_0 is not zero the wing undergoes a static deflection and a perturbation solution about a nonzero (nontrivial) static deflection must be used to determine the flutter condition.

Let

$$\bar{q}_o = \bar{q}_o^s + \hat{\bar{q}}_o,\ \bar{a}_m = \bar{a}_m^s + \hat{\bar{a}}_m,\ \bar{b}_n = \bar{b}_n^s + \hat{\bar{b}}_n,\quad \gamma = \gamma^s + \hat{\gamma}, \tag{18}$$

where the superscript s quantities represent static equilibrium states and the hat quantities the dynamic perturbed states. If Eq. (18) is substituted into the nonlinear aeroelastic state-space equations and only first order terms in the perturbed variables are kept, a set of dynamic perturbation equations are found. This set of equations has a structural stiffness matrix which is now a function of the static equilibrium deformation. The eigenvalue problem for the nonzero angle of attack case can now be solved using this new set of aeroelastic state-space equations. See Tang and Dowell (2001) for more details of this procedure.

The perturbation solution can also be used to determine the increase in the structural natural frequencies of the plate due to some prescribed static loading. For example, this phenomenon will occur when the wing undergoes a static deflection due to an initial angle of attack. Bench tests were performed to assess the nonlinear structural model and the perturbation theory for different levels of static deflection due to a static gravity loading of the wing plate. By rotating the plate relative to the gravity vector, gravity loadings from 0 to 9.81 m/s^2 were obtained. Figs. 4 and 5 present results for the experiment as well as the perturbation solution and an ANSYS solution using a nonlinear prestress model available in that package. The experimental results presented in Figs. 4 and 5 are uncertain within ± 0.05 Hz. As one can see, the theoretical results using the perturbation solution are in quite good agreement with the experimental data. Note also the small increase in the natural frequency of the wing. At a 1 g static load the maximum static deflection is about 4 plate wing thicknesses. The relatively small increase of the first natural frequency at this level of static deflection shows that the wing has a relatively modest stiffening at this deflection level due to nonlinear effects. This will be discussed further when the flutter and limit cycle results are shown. It is noted here that the underlying theory in ANSYS is for a quasi-three-dimensional shell element and thus there is expected to be some difference between results obtained from ANSYS per se and the von Karman plate theory. Of course, ANSYS is used to find the structural eigenmodes for the von Karman/Lagrangian model.

3. Experimental methods: flutter and LCO

The experimental investigation of flutter and LCO was performed in the Duke University wind tunnel. Fig. 6 displays a schematic of the apparatus (not to scale). The wing is fixed at its root chord (middle 60%) by two steel brackets which

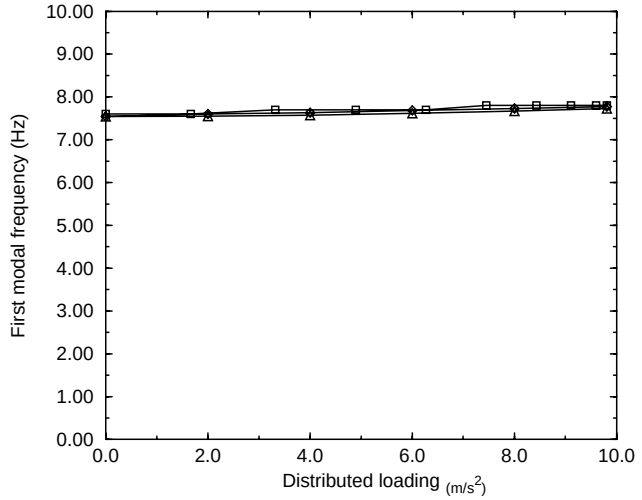

Fig. 4. First structural natural frequency of the wing for different static gravity loading levels: △–△, perturbation; □–□, experimental; ◇–◇, ANSYS nonlinear prestress analysis.

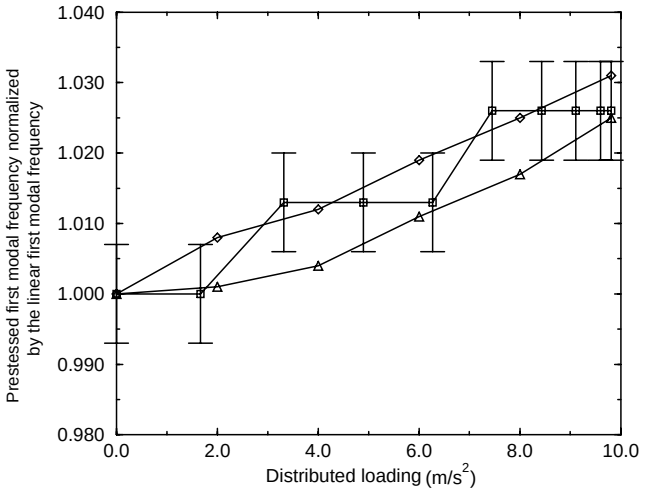

Fig. 5. Increase of the plate first natural frequency under differing levels of distributed gravity loading. The vertical bar is the uncertainty in the measured data point: △–△, perturbation; □–□, experimental; ◇–◇, ANSYS nonlinear prestress analysis.

are attached to the wing with five screws. The brackets and wing are then clamped into a vise which is attached to a heavy, grounded table. This root fixture is placed underneath the wind tunnel such that only the wing portion is in the tunnel. The apparatus is not attached to any portion of the tunnel. This was done so that any tunnel vibrations would not contaminate the wing vibration data.

In order to collect vibration data, an accelerometer was placed near the tip of the wing. This was accomplished by drilling a small hole near the tip and then attaching the accelerometer with an adhesive. The accelerometer was operated in velocity mode which gave results with the least amount of noise. In order to obtain accurate measurements of the displacement signal with multiple frequencies, a calibration was performed where the displacement of a 1 cycle piston was set a priori and then the velocity data were read from the accelerometer. A strain gauge was placed near the root chord in order to give some estimate of the static deflection at the tip when the plate was placed at an initial angle of attack and is statically deflected. Another calibration was performed that measured the strain at the root chord when the tip underwent a deflection of known magnitude due to some prescribed static load. Using this calibration will not give exact results for the measurement of the static displacement of the wing due to an initial angle of attack, but it is accurate enough to give a good estimate of the order of magnitude of the deflection.

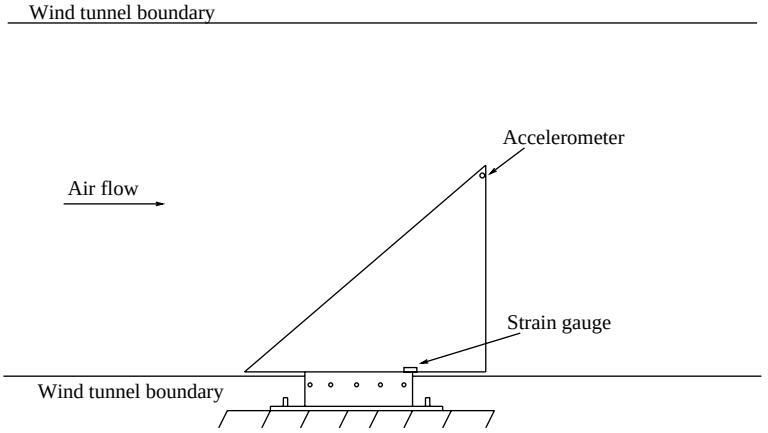

Fig. 6. Schematic of the experimental apparatus.

Table 1
Zero steady angular of attack flutter velocity for varying levels of structural modal damping

Modal damping $\xi_{1..nxy}$	Flutter velocity (m/s)	Flutter frequency (Hz)
0.00	38.1	25.1
0.02	40.8	24.2
0.04	42.5	23.5
0.06	44.2	23.0
0.08	45.4	22.5
0.10	46.5	22.1
0.12	47.4	21.9
0.14	48.4	21.6

The accelerometer data acquisition during each wind tunnel experiment was performed with standard Labview software. The strain gauge data were read from the strain gauge electrical circuit directly.

Five angle of attack cases were examined, from 0° to 4° in 1° increments. The test procedure used was to fix the initial angle of attack and then increase the wind tunnel flow velocity. The flow velocity range was 10–52 m/s.

4. Theoretical and experimental results

The wing configuration is a 45° delta made from 0.24 cm thick plastic (Lucite) material. This wing is clamped along the middle 60 percent of the root chord (23 cm). The Poisson ratio is 0.45 and the structural damping (ξ_o) used in the theoretical model for each mode is 0.04 based upon experimental decay measurements made in vacuo. Table 1 shows the zero steady angle of attack flutter velocity for varying levels of ξ_o. There is a moderate sensitivity of the flutter velocity to the level of the structural damping. Table 2 displays the important input parameters that are used in the numerical simulation and experimental study.

In the analysis, the number of out-of-plane and in-plane structural modes was $nxy = 10$ and $mxy = 600$, respectively. Table 3 displays the first 10 theoretical as well as five measured experimental structural natural frequencies. Generally good agreement is found. The theoretical natural frequencies are the values that are used in the generalized linear stiffness and damping terms in the aeroelastic model.

Two sets of root chord in-plane boundary conditions were considered in the theoretical model, zero in-plane restraint and clamped in-plane restraint. Since the true in-plane restraint that is present in the experimental model is not actually known, these two cases represent the two extreme situations and the true experimental boundary condition most likely falls somewhere between these two. Flutter results for both cases will be presented.

Table 2
Input parameters used in the numerical study

Structural parameters	Fluid parameters
$\rho = 1145\,\mathrm{kg/m^3}$	$\rho_\infty = 1.225\,\mathrm{kg/m^3}$
$v = 0.45$	$kmn = 120$
$E = 3.3 \times 10^9\,\mathrm{N/m^2}$	$knx = 645$
$h = 0.00239\,\mathrm{m}$	$Ra = 7$
$a = 0.381\,\mathrm{m}$	The wake length in the vortex lattice model is 2.33 root chord lengths
$b = 0.381\,\mathrm{m}$	
$nxy = 10$	
$mxy = 600$	
$\xi_o = 0.04$	

Table 3
Theoretical and experimental plate modal frequencies (Hz)

Theoretical	Experimental
7.54	7.50
30.00	29.26
34.58	33.37
71.35	68.03
86.18	84.54
109.39	
136.26	
148.23	
156.82	
186.56	

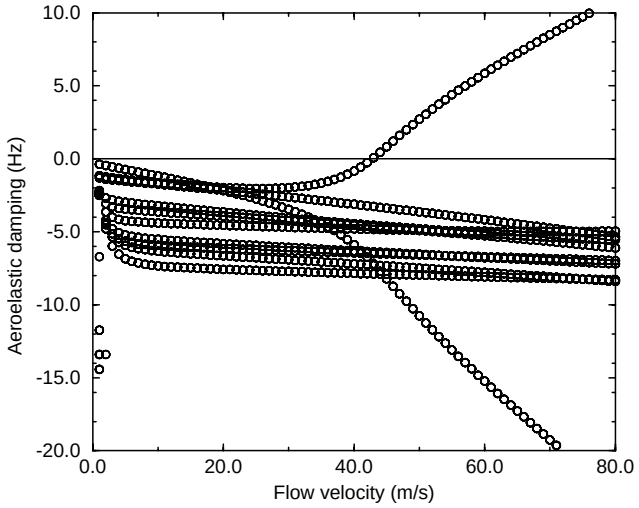

Fig. 7. Aeroelastic stability results for zero steady angle of attack: aeroelastic damping versus flow velocity.

4.1. Flutter results

For nonzero steady angle of attacks, the perturbation solution technique is used where the static states are extracted from the steady nonlinear response. This steady or static nonlinear response is found using a direct time-marching solution of the full nonlinear aeroelastic model. The flutter results for both zero and nonzero angles of attack can be confirmed by time-marching these same equations and noting when the response approaches an LCO.

Results from the eigenvalue solution for the zero angle of attack case is shown in Fig. 7. It shows the real part of the aeroelastic eigenvalue or damping versus the flow velocity. The flutter velocity is 42.8 m/s and the corresponding flutter frequency is 23.1 Hz. Once above the flutter velocity, the system remains unstable, i.e., there is no upper flutter boundary for all of the flutter results presented here. For all of the angles of attack studied here, flutter occurs along with a coalescence of the first bending and first torsion aeroelastic modal frequencies. The first aeroelastic torsion mode is the one that becomes unstable. This is shown in Fig. 8 which is a root-locus plot for zero angle of attack. Since there is no increase in stiffness due to a static deflection for zero angle of attack, the in-plane boundary condition does not have any effect on the flutter solution.

Fig. 9 displays the flutter solutions when the steady angle of attack is 2° and 4°. For comparison, the zero angle of attack case is also shown. For a steady angle of attack of 2°, the zero in-plane constraint model has a flutter velocity of 46 m/s while the full in-plane constraint flutter velocity (solution not shown in Fig. 9) is 58.5 m/s. The reason for the increase in flutter velocity from the zero angle of attack result can be understood as follows. For a steady angle of attack, the wing undergoes a static deflection. This deflection then creates a tension in the wing and with it comes an increase in the structural stiffness and natural frequencies of the wing. Recall the type of flutter that is seen here is a

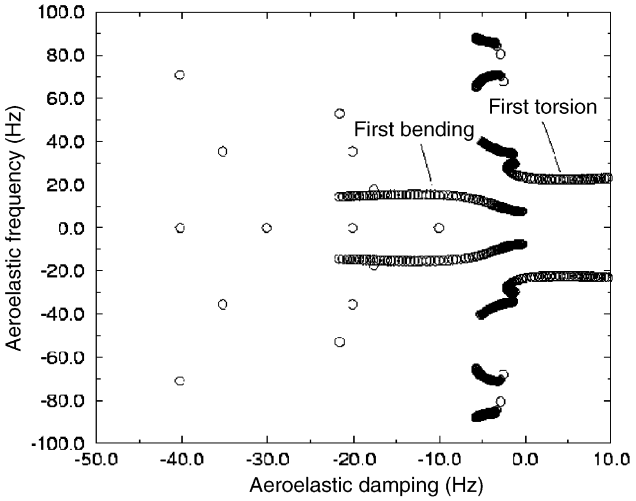

Fig. 8. Root–locus plot for zero steady angle of attack.

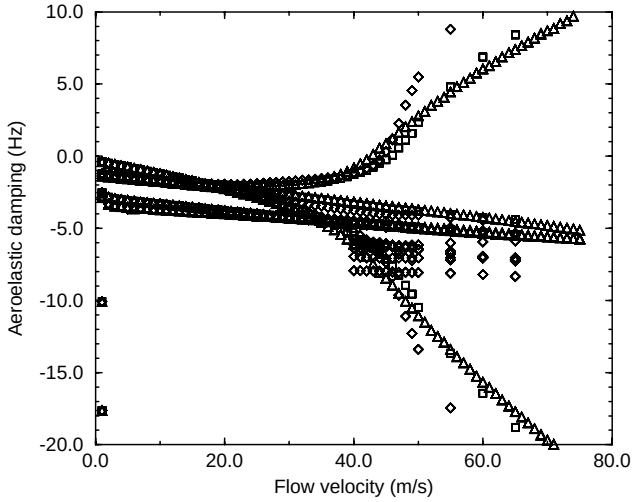

Fig. 9. Aeroelastic stability results for the wing at nonzero steady angles of attack: △, $\alpha = 0°$; □, $\alpha = 2°$; ◇, $\alpha = 4°$.

coalescence flutter with primary contributions from the first bending and first torsion modes. One procedure that is often used to increase the flutter velocity of a wing that undergoes flutter of this type is to add stiffness such that the first torsion mode natural frequency increases more than that of the first bending mode. Since the flutter here is dependent on the coalescing of the two modes, this separation of the frequencies due to nonzero angle of attack causes the flutter speed to increase. It turns out that the additional stiffness from the static deflection is such that the torsion mode frequency increases more than the bending mode, and therefore the flutter velocity increases as does the flutter frequency for an angle of attack of 2°. This is seen in both the zero in-plane constraint model and full in-plane constraint model. However, the degree to which the flutter velocity increases is much larger for the "stiffer" full in-plane constraint model than the zero in-plane constraint. For a steady angle of attack of 4°, different qualitative results are found for the two different in-plane constraint models. For the zero in-plane constraint, the flutter velocity decreases from 46 m/s at a 2° angle of attack to 44.1 m/s at 4°. The reason for this is that for the large static deflection (around 20 plate thicknesses) the first bending modal frequency now shows a larger increase than the first torsion modal frequency.

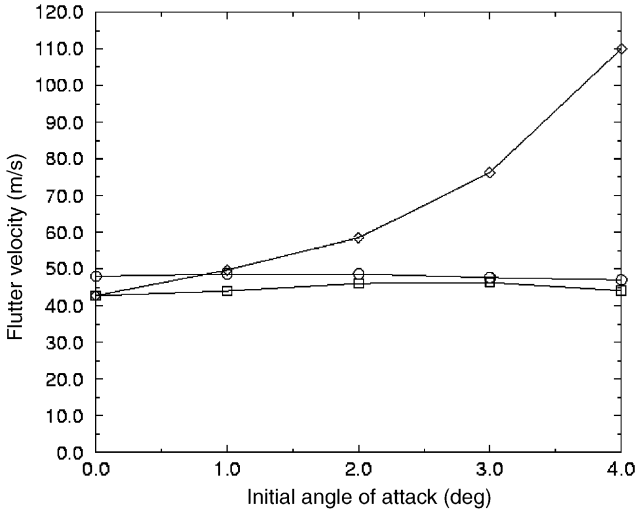

Fig. 10. Flutter velocity as a function of steady angle of attack: ◦, experimental; □, theoretical with no root chord in-plane constraint; ◇, theoretical with full root chord in-plane constraint.

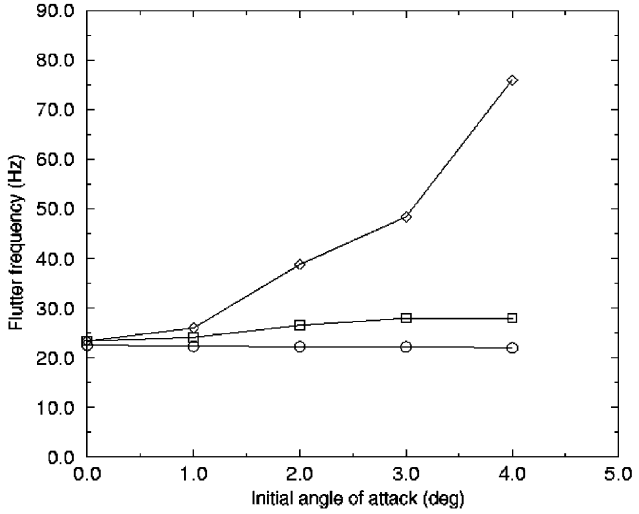

Fig. 11. Flutter frequency as a function of steady angle of attack: ◦, experimental; □, theoretical with no root chord in-plane constraint; ◇, theoretical with full root chord in-plane constraint.

This brings the frequencies closer together and hence the flutter velocity drops. For the stiffer, full in-plane constraint wing, the bending and torsional frequencies spread apart and we once again see an increase in flutter velocity to 110.0 m/s.

Figs. 10 and 11 display the flutter velocity and frequency, respectively, versus the steady angle of attack for the two in-plane constraint cases and the experimentally determined flutter results. The qualitative and quantitative agreement between theory and experiment for the flutter velocity results are quite good for the theoretical model with zero in-plane constraint, but the theory for a full in-plane constraint is in much poorer agreement with experiment. Both the experiment and the theoretical models for soft in-plane support show a slight increase in flutter velocity at lower angles of attack and then a decrease at higher angles of attack. The corresponding flutter frequency results agree less well with the experimental flutter frequency dropping slightly as the angle of attack is increased while the theoretical zero in-plane constraint model shows a slight increase as the angle of attack increases.

By contrast, the theoretical model with the full in-plane constraint appears to be much too "stiff" in that the degree of nonlinearity that it shows does not seem to match that of the experiment. For this theoretical model, the flutter

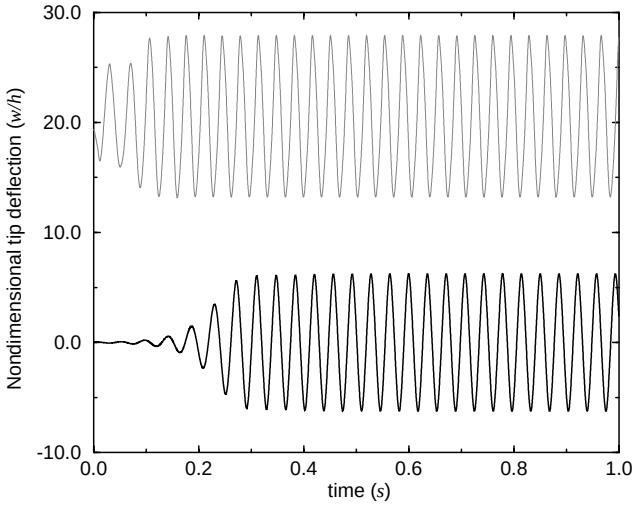

Fig. 12. Theoretical limit cycle time histories at 52.2 m/s: nondimensionalized tip deflection.

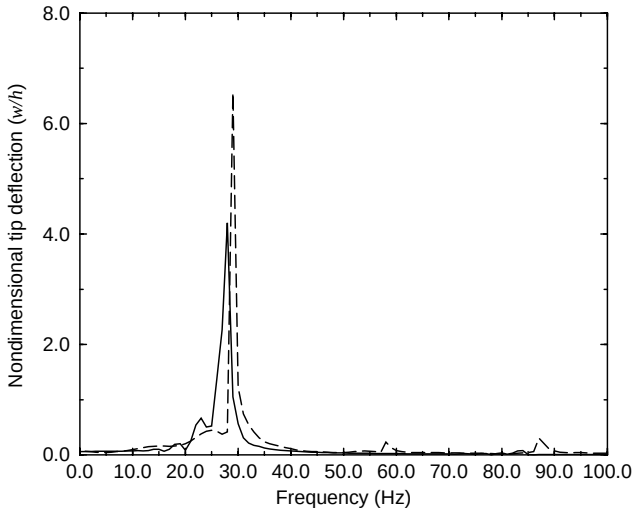

Fig. 13. Theoretical FFT results for flow at 52.2 m/s: nondimensionalized tip deflection; —— , 0° steady angle of attack; – – – , 3° steady angle of attack.

velocity increases significantly as the angle of attack is increased as does the flutter frequency for the "stiff" theoretical in-plane boundary condition.

4.2. Limit cycle results

A standard discrete time algorithm was used to calculate the limit cycle results for the aeroelastic system. For a constant velocity U, the time step Δt is chosen to be such that $U(\Delta t/\Delta x) = 1/15$. A limit cycle is observed when the flow velocity is above the flutter velocity determined by the perturbation flutter velocity. All of the theoretical results presented below will be for the zero in-plane constraint model.

Fig. 12 is a typical time history of the nondimensionalized deflection near the wing tip for the theoretical model at 0° and 3° steady angles of attack at 52.2 m/s. This flow velocity is above the perturbation flutter velocity for both cases. Fig. 13 is the corresponding FFT for the aeroelastic responses. Figs. 14 and 15 are the corresponding experimental

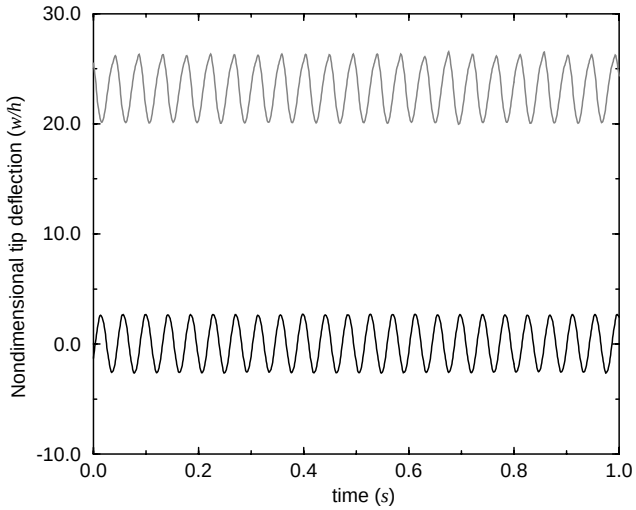

Fig. 14. Experimental limit cycle time histories at 52.2 m/s: nondimensionalized tip deflection.

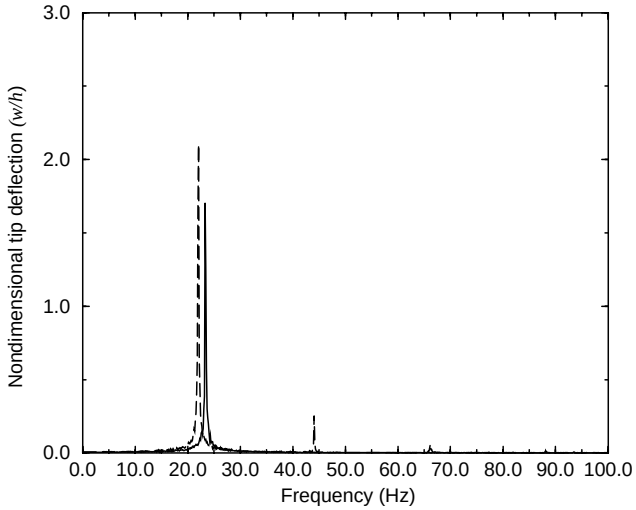

Fig. 15. Experimental FFT results for flow at 52.2 m/s: nondimensionalized tip deflection; ——, 0° steady angle of attack; – – –, 3° steady angle of attack.

results for this flow velocity and angles of attack. The static deflection predicted by the theoretical model and measured experimentally is quite large when the steady angle of attack is 3°, i.e., $w_{\text{static}}/h \approx O(10^1)$. Even so, the assumption of the von Karman plate theory that the square of the plate slopes ($\partial w/\partial y$ and $\partial w/\partial x$) be much less than 1 still holds. The frequency response data show higher harmonic content in both the experiment and theory for the non zero angle of attack data. The theoretical response contains both the second and third harmonic in equal amounts while the experiment has mostly a second harmonic.

Recall that the effect of the static deflection and stiffness that it induces is quadratic in the dynamic deflection. This can be shown through the perturbation analysis (see Tang and Dowell (2001)). This quadratic dependence is what causes the second harmonic to appear. The third harmonic is a direct consequence of the cubic nonlinearity that is present in the plate equations. In examining the experimental data and noting the fact that the second harmonic is the main higher harmonic, one can surmise that at this static deflection and LCO magnitude, the static deflection is the

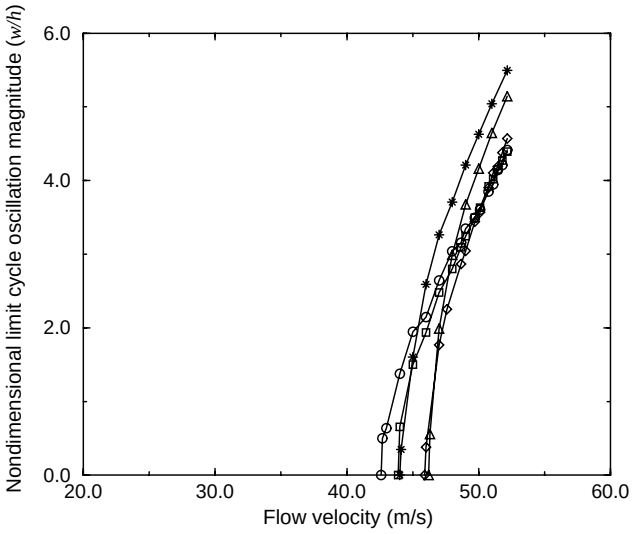

Fig. 16. Theoretical limit cycle tip deflection magnitudes versus flow velocity for various steady angles of attack: ∘–∘, $\alpha = 0°$; □–□, $\alpha = 1°$; ◇–◇, $\alpha = 2°$; △–△, $\alpha = 3°$; ∗–∗, $\alpha = 4°$.

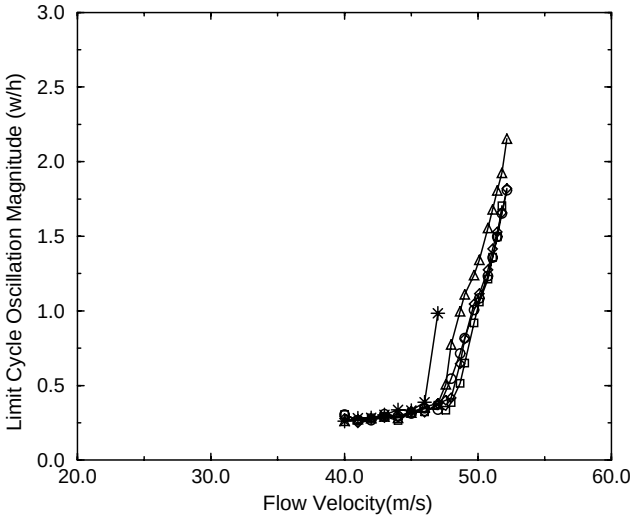

Fig. 17. Experimental limit cycle tip deflection magnitudes versus flow velocity for various steady angles of attack: ∘–∘, $\alpha = 0°$; □–□, $\alpha = 1°$; ◇–◇, $\alpha = 2°$; △–△, $\alpha = 3°$; ∗–∗, $\alpha = 4°$.

main contributor in determining the nonlinear effects that are present in the response. The dynamic nonlinearity, which is cubic, is not as strong at this limit cycle magnitude which is about 2 thicknesses.

Another point of interest is that in both the experiment and the theory, the limit cycle magnitude is larger for the 3° angle of attack than for the 0° angle of attack. This effect can be seen more clearly in Figs. 16–18 which are plots of the limit cycle tip deflection magnitude versus flow velocity for different steady angles of attack. As one can see for all of the theoretical cases, as the angle of attack is increased the limit cycle magnitude at a given flow velocity also increases. This effect is also present for the experimental data. Fig. 18 is a comparison of theory and experiment for the limit cycle magnitude versus flow velocity. The flow velocity in this plot is normalized by the appropriate flutter velocity.

It should be emphasized that while the onset of flutter and LCO can be precisely determined in the theoretical model, because of some inevitable turbulent fluctuations in the wind tunnel flow field, the velocity at which flutter and LCO begin cannot be as precisely determined in the experiment. This may account for some of the apparent differences between theory and experiment.

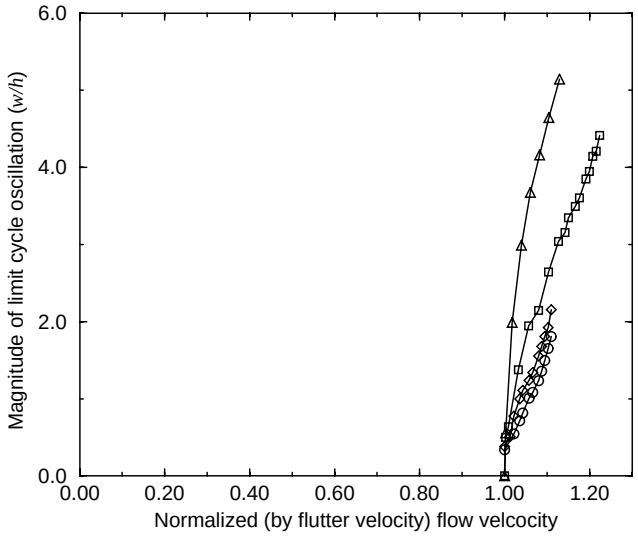

Fig. 18. Theoretical and experimental comparison of normalized limit cycle tip deflection magnitudes: ○–○, experiment at $\alpha = 0°$; □–□, theoretical at $\alpha = 0°$; ◇–◇, experiment at $\alpha = 3°$; △–△, theoretical at $\alpha = 3°$.

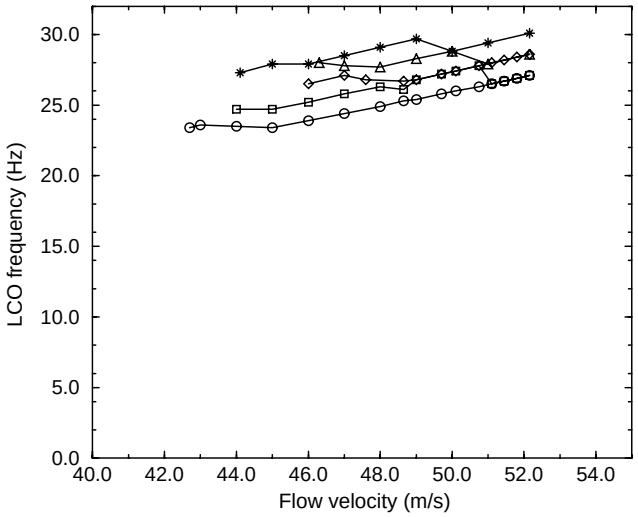

Fig. 19. Theoretical LCO frequency: ○–○, $\alpha = 0°$; □–□, $\alpha = 1°$; ◇–◇, $\alpha = 2°$; △–△, $\alpha = 3°$; ∗–∗, $\alpha = 4°$.

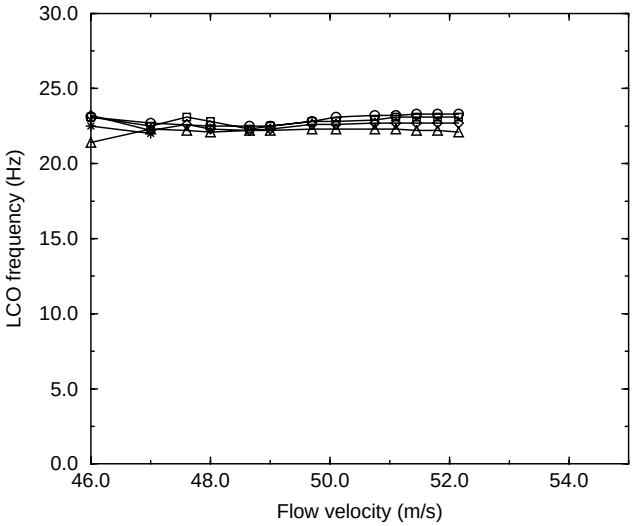

Fig. 20. Experimental LCO frequency: ○–○, $\alpha = 0°$; □–□, $\alpha = 1°$; ◇–◇, $\alpha = 2°$; △–△, $\alpha = 3°$; ∗–∗, $\alpha = 4°$.

The theoretical model appears stiffer than the experimental model from the results shown in Fig. 18. The higher nonlinear stiffness of the theory is also evident when one looks at Figs. 19 and 20 which show the response frequency versus the flow velocity. For each theoretical case, the limit cycle frequency increases with both angle of attack and flow velocity while the experiment actually shows a very slight decrease in frequency with an increase in angle of attack. Neither the experimental nor theoretical models show a significant change in limit cycle frequency with flow velocity, however.

5. Conclusions

The present theoretical and experimental results provide some insight into the nonlinear aeroelastic behavior of a partially clamped, cantilevered delta wing at low angles of attack in low subsonic flow. Using a linear reduced order aerodynamic model and nonlinear structural model, flutter and LCO results were compared to experiment and found to agree reasonably well qualitatively. Both the experiment and theory (with soft in-plane boundary conditions) display an increase and then a decrease in the flutter speed as the angle of attack is increased, as well as an increase in the magnitude of the LCO at a given velocity as the angle of attack is increased. Results from both the theory and the experiment show a more modest degree of nonlinearity for the delta wing model clamped along a single (root) edge as compared to plates that are clamped on all edges (Dowell, 1975), as expected. However, the appropriate scaling for the nonlinear static deflections and nonlinear dynamic deflections (LCO) is still the plate thickness (rather than say wing chord) as is true for panels with two or more edges fixed.

It is noted that nonlinear vortex models such as that developed by Mook and his colleagues (see Lutton and Mook (1993); Hall et al., 2001) could be used to investigate nonlinear aerodynamic effects. These may be most important near the tip of the delta wing and/or if leading edge vortices are formed for a sufficiently large angle of attack. Such a study would be an important next step in investigating further the aeroelastic phenomena discussed in the present paper.

Finally, the very recent and important work of Gordnier (2002) should be cited. In that paper, a theoretical correlation with earlier experimental results by Schairer and Hand (1997) for a plate-like delta wing in a transonic flow has been made. It is also demonstrated that the dominant nonlinearity is the structural effect studied in the present paper and that for a sufficiently thin delta wing the aerodynamic nonlinear effects are less significant even in the transonic flow regime.

Acknowledgements

This work was supported by AFOSR Grant, "Dynamics and Control of Nonlinear Fluid–Structure Interaction". Dr Dan Segalman and Dr Dean Mook are the AFOSR Program Managers.

References

ANSYS User Manual, 1998, Release 5.5.1. Swanson Analysis Systems, Inc. Canonsburg, PA, USA.

Doggett, R.V., Solstmann, D.L., 1989. Some low-speed flutter characteristics of simple low-aspect-ratio delta wing models. NASA TM 101547.

Dowell, E.H., 1975. Aeroelasticity of Plates and Shells. Kluwer Publishers, Dordrecht.

Gordnier, R.E., 2002. Computation of limit cycle oscillations of a delta wing. AIAA Paper 2002-1411.

Hall, B.D., Mook, D.T., Nayfeh, A.H., Preidikman, S., 2001. Novel strategy for suppressing the flutter oscillations of aircraft wings. AIAA Journal 39, 1843–1850.

Hall, K.C., 1994. Eigenanalysis of unsteady flows about airfoils, cascades and wings. AIAA Journal 32, 2426–2432.

Katz, J., Plotkin, A., 2001. Low Speed Aerodynamics, 2nd Edition. Cambridge University Press, Cambridge.

Lutton, J.A., Mook, D.T., 1993. Numerical simulations of flutter and its suppression by active control. AIAA Journal 31, 2312–2319.

Schairer, E.T., Hand, C.A., 1997. Measurement of unsteady aeroelastic model deformation by stereo photogrammetry. AIAA Paper 1997-2217.

Tang, D., Dowell, E.H., Hall, K.C., 1999a. Limit cycle oscillations of a cantilevered wing in low subsonic flow. AIAA Journal 37, 364–371.

Tang, D., Henry, J.K., Dowell, E.H., 1999b. Limit cycle oscillations of delta wing models in low subsonic flow. AIAA Journal 37, 1355–1362.

Tang, D., Dowell, E.H., 2001. Effects of angle of attack on nonlinear flutter of a delta wing. AIAA Journal 39, 15–21.

Weiliang, Y., Dowell, E.H., 1991. Limit cycle oscillations of a fluttering cantilever plate. AIAA Journal 29, 1929–1936.